

Emergence of dynamic vortex glasses in disordered polar active fluids

Amélie Chardac,¹ Suraj Shankar,² M. Cristina Marchetti,³ and Denis Bartolo¹

¹*Univ. Lyon, ENS de Lyon, Univ. Claude Bernard,
CNRS, Laboratoire de Physique, F-69342, Lyon, France*

²*Department of Physics, Harvard University, Cambridge, MA 02318, USA*

³*Department of Physics, University of California Santa Barbara, Santa Barbara, CA 93106, USA*
(Dated: August 6, 2022)

In equilibrium, disorder conspires with topological defects to redefine the ordered states of matter in systems as diverse as crystals, superconductors and liquid crystals. Far from equilibrium, however, the consequences of quenched disorder on active condensed matter remain virtually uncharted. Here, we reveal a state of strongly disordered active matter with no counterparts in equilibrium: a dynamical vortex glass. Using high-content microfluidic experiments, we show how colloidal flocks can collectively cruise through disorder without relaxing the topological singularities of their flows. The resulting state is dynamical with locally correlated flows, but the velocity patterns are stationary and exponentially degenerated, shaped by a finite density of frozen vortices. We establish theoretically that quenched isotropic disorder acts as a random gauge field capable of nucleating orientational topological defects thereby turning active liquids into dynamical vortex glasses. Beyond colloidal active matter, we argue that this robust mechanism should shape the collective dynamics of a broad class of disordered active matter, from synthetic active nematics to collections of living cells exploring heterogeneous media.

From a physicist perspective, flocks are ensembles of living or synthetic motile units collectively moving along a common emerging direction [1–4]. They realize one of the most robust ordered states of nonequilibrium matter observed over five orders of magnitude in scale and in systems as diverse as motility assays, self-propelled colloids, shaken grains and actual flocks of birds [3, 5–10]. The quiet flows of flocks are in stark contrast with the spatio-temporal chaos consistently reported and predicted in active nematic liquid crystals, another abundant form of ordered active matter realized in biological tissues, swimming cells, cellular extracts and shaken rods [2, 11]. Active nematics do not support any form of long range order [4, 12]. Their structure is continuously bent and destroyed by the proliferation and swarming motion of singularities in their local orientation: topological defects [11, 13–15]. Unlike in active nematics, topological defects in flocking matter are merely transient excitations which annihilate rapidly and allow uniaxial order to extend over system-spanning scales [4].

This idyllic view of the ordered phases of active liquids is limited, however, to pure systems. Disorder is known to profoundly alter the stability of topological defects and the corresponding ordered states in equilibrium condensed matter [16–18], but its role in active fluids remains virtually uncharted territory. All previous studies [19–26], including our own early experiments [22], have been limited to weak disorder and smooth perturbations around topologically trivial states. Unlike in equilibrium, *disorder-induced* topological excitations have been out of reach of any active-matter experiment, theory and simulations.

In this article we show how isotropic disorder generically challenges the extreme robustness of flocking matter to topological defects. We map the full phase behavior of colloidal flocks in disordered environments and re-

veal an unanticipated state of active matter: a dynamical vortex glass (DVG). In DVGs, millions of self-propelled particles can steadily cruise through disorder maintaining local orientational order and without relaxing the topological singularities of their flows. The associated flow patterns are exponentially degenerated and shaped by amorphous ensembles of frozen topological defects, yielding a *dynamical* state akin to the *static* vortex-glass phase of dirty superconductors and random-gauge magnets [27–29]. Extending the theory of flock hydrodynamics beyond the spin-wave approximation, we uncover a novel activity-induced random *gauge* field that elucidates the emergence and stabilization of topological vortices by quenched disorder. Finally, we discuss the universality of the DVG phase beyond the specifics of polar active matter and colloidal flocks.

I. EXPERIMENTAL SYSTEM

Our experiments are based on the model system we introduced in [6]. We use Quincke rotation to power inanimate polystyrene beads of radius $a = 2.4 \mu\text{m}$ [30, 31], and turn them into colloidal rollers self-propelling at constant speed $\sim 1 \text{ mm/s}$ in circular microfluidic chambers of radius $R = 1.5 \text{ mm}$, see Movie S1. Before addressing the impact of disorder on their collective dynamics, it is worth recalling the phenomenology of the pure ordered phase [32, 33]. As the rollers are set in motion, they interact and self-assemble into a spontaneously flowing liquid equivalently referred to as a flock, a Toner–Tu fluid, or a polar liquid [2, 34] shown in Movie S1. The resulting flow patterns are initially isotropic and marred by a number of ± 1 topological defects clearly visible in the Schlieren patterns of Fig. 1a and Movie S2. However, the velocity-alignment interactions responsible for flock-

ing motion penalize flow distortions thereby causing the attraction and annihilation of defects of opposite charge. The resulting lively coarsening dynamics lasts few tens of seconds and ultimately yields pristine azimuthal flows *with long-range order in two dimensions*, Fig. 1a.

To comprehensively investigate how disorder alters the phases of polar active matter, we perform high-content experiments on the microfluidic device sketched in Fig. 1b. On a single chip, we quantify the flows of disordered roller fluids in 32 different disordered geometries. Disorder is implemented in 3 mm wide circular chambers decorated by random arrays of isotropic obstacles of diameter $10\ \mu\text{m}$ that repel the rollers at a distance, while leaving their speed unaltered, see Fig. 1c and Movie S3. We replicate the experiments increasing the obstacle fraction Φ_o from 0% to 38% keeping the system below the Lorentz localization transition of individual rollers [35, 36]. All experiments are systematically performed for several disorder realizations and initial conditions, see also Methods.

Let us first discuss the impact of disorder on a polar liquid deep in the flocking phase, for $\rho_0 = 7 \pm 0.5 \times 10^{-2}$. For small disorder, $\Phi_o < 9\%$, the obstacles hardly disrupt the collective flow, as ± 1 defects formed at the onset of collective motion quickly annihilate and the system coarsens to an ordered flocking state which, in the disc geometry, takes the form of single a large vortex (+1 defect, see Fig. 1 and Movie S4). In stark contrast, increasing Φ_o above 9%, a very distinct type of organization emerges. Disorder essentially arrests the coarsening by pinning ± 1 defects. While the global flow is zero, we find locally correlated flows through meandering patterns bent by disorder (Fig. 1d and Movie S5). Particles stream coherently through the meanders, resulting in a finite correlation length for orientational order, but the structure of the flow network itself is static and fixed in space, as shown in Fig. 1d and Movie S6. Further increasing the obstacle fraction (above 26%), we recover the liquid-gas transition reported in [22]. In the gas phase, particles are motile, but there is no orientational order as defect pairs continuously unbind and annihilate as seen in Figs. 1d, 1e and Movie S7. The two transitions between the three dynamical states are unambiguously determined by the variations of $\mathcal{N}(\Phi_o)$, the mean number of topological defects in the velocity field, plotted in Fig. 1f (the detection of the topological defects is detailed in Supplementary Note II). The emergence of meandering flows is signalled by the linear increase of \mathcal{N} as Φ_o exceeds the critical value $\Phi_c = 9\%$, whereas the loss of local orientational order saturates $\mathcal{N}(\Phi_o)$ above $\Phi_o = 26\%$.

II. OBSERVATION OF THREE DISTINCT PHASES: FLOCK, MEANDERS AND GAS

In order to quantitatively distinguish the dynamics in the three regimes, we inspect the statistics of the time-averaged polarization defined as $\mathbf{p}(\mathbf{r}) = \langle \hat{\mathbf{v}}(\mathbf{r}, t) \rangle_t$, where the unit vector $\hat{\mathbf{v}}(\mathbf{r}, t)$ is the instantaneous orientation of the velocity field, see Methods. The distributions of

$\mathbf{p}(\mathbf{r})$ in Fig. 2a show that, for small disorder, the flow is uniformly polarized along the azimuthal direction, which reflects nearly perfect polar order. Conversely, above Φ_c global polar order is suppressed, and the polarization is isotropically distributed on the scale of the system. The strong localization of the distribution on the unit circle demonstrates, however, that meanders persistently distort the streamlines *without* arresting the local flows. Above $\Phi_o = 26\%$, in the active-gas phase, the typical polarization vanishes, polar order melts and flows are suppressed at all scales.

We now demonstrate that the two flowing patterns correspond to two distinct dynamical phases of active matter. We first stress that polar liquids with genuine long range orientational order survive at finite disorder (see also Supplementary Note VB). Unlike active nematics, deconfining the system does not suppress the stationary vortex patterns shown in Fig. 1d [37–39]. This crucial result follows from the finite-size analysis of the polarization order parameter $\mathcal{P}(\ell) = \sqrt{\langle p_r(\mathbf{r}) \rangle_{\mathbf{r}}^2 + \langle p_\theta(\mathbf{r}) \rangle_{\mathbf{r}}^2}$, where ℓ is the size of the region where spatial averaging is performed. This definition of \mathcal{P} is natural in a circular geometry where the spatial average of \mathbf{p} vanishes, even in pure systems. Below Φ_c , Extended Data Fig. 1 clearly indicates that $\mathcal{P}(\ell)$ converges to a finite value over a finite length scale $\xi_{\mathcal{P}}$, signalling long range polar order. Conversely, deep in the meandering regime $\mathcal{P}(\ell)$ vanishes over a finite scale. Polar liquids and meanders are therefore two genuinely distinct phases of active matter.

The transition between these two dynamical phases is captured by the global polarization $\mathcal{P} \equiv \mathcal{P}(\ell = 2R)$, where R is the chamber radius. We can see in Fig. 2b that \mathcal{P} decays weakly and linearly with Φ_o for small disorder, but drops sharply to 0 at the critical value Φ_c defined from the proliferation of quenched topological defects in Fig. 1f. The bifurcation of \mathcal{P} in Fig. 2b suggests a critical scenario. This hypothesis is further supported by Fig. 2c which reveals a divergence, or at the very least a drastic increase of the correlation length $\xi_{\mathcal{P}}$ at the onset of meandering motion. The polarization \mathcal{P} alone, however, does not distinguish the meander from the gas phase. We thus introduce the Edwards–Anderson parameter $\mathcal{Q}_{\text{EA}} = \langle \hat{\mathbf{v}}(\mathbf{r}, t) \cdot \hat{\mathbf{v}}(\mathbf{r}, t + T) \rangle_{\mathbf{r}, t, T \rightarrow \infty}$ that quantifies the temporal persistence of the emergent flows [40]. The finite non-zero value of \mathcal{Q}_{EA} for $\Phi_c < \Phi_o < 26\%$ (Fig. 2b) confirms the persistence of polar order along the meanders. We also find that the continuous transition, or crossover, between the meander and the gas phase, where $\mathcal{Q}_{\text{EA}} \sim 0$, coincides with that identified from the topological defect statistics in Fig. 1f.

Taking advantage of our high-content microfluidic experiments, we measure \mathcal{P} and \mathcal{Q}_{EA} in more than 400 experiments performed varying the roller fraction from 10^{-3} to 1.5×10^{-1} , and Φ_o from 0 to 38% for multiple disorder realizations and initial conditions. The resulting phase diagram shown in Fig. 2d firmly establishes that disorder and topological defects do not merely offset the flocking transition as reported in [22], but conspire to

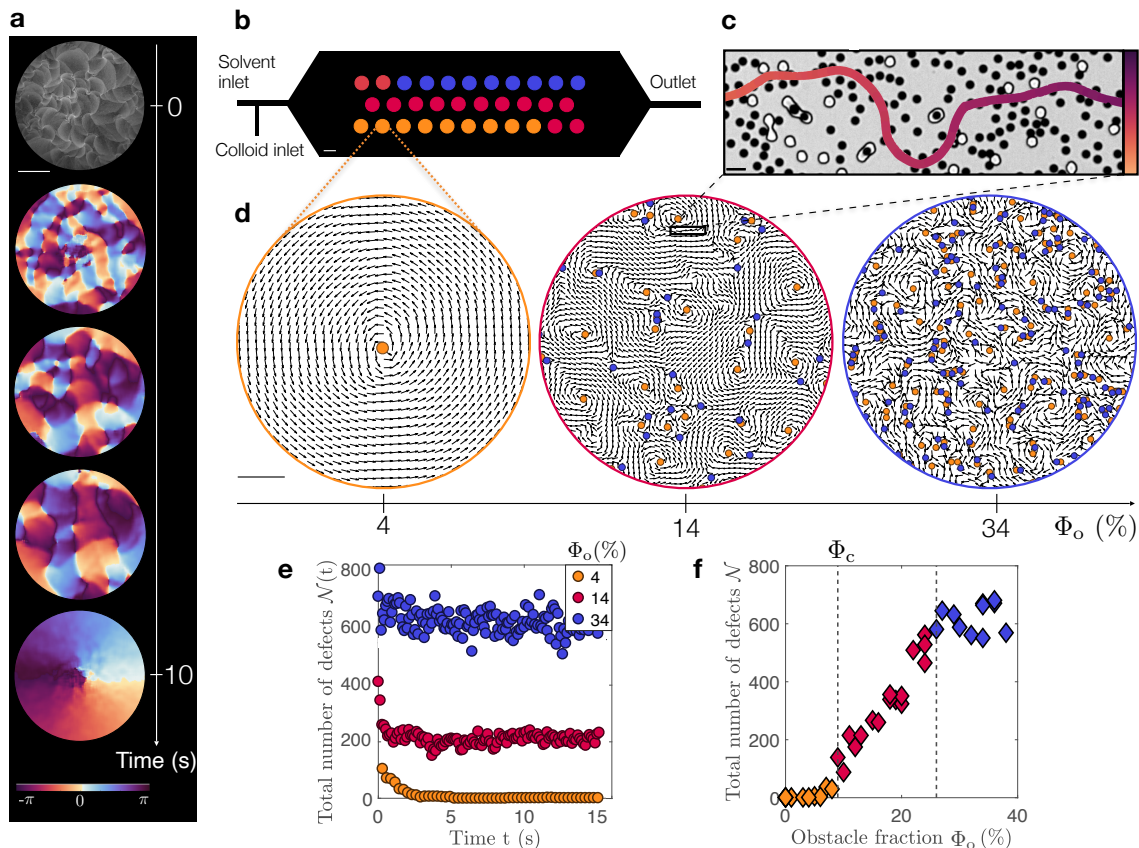


FIG. 1. **Emergence and destruction of polar flows.** **a**, Experimental picture of a Quincke-roller fluid at the onset of self-propulsion and subsequent Schlieren patterns of the flow field. The colormap indicates the angle of the local velocity field with the x -axis. The many topological defects formed at the onset of collective motion coarsen yielding a pristine azimuthal flow. Scale bar: 1 mm. **b**, Schematics of the microfluidic device. 32 circular chambers are patterned with random lattices of circular obstacles. Each chamber correspond to a different value of Φ_o . A T-junction makes it possible to continuously vary the packing fraction of Quincke rollers in all chambers at once. Same color coding as in **f**. Scale bar: 3 mm. **c**, Closeup picture showing Quincke rollers collectively moving through a disordered lattice of micro-fabricated obstacles. A roller trajectory shows that the obstacles repel the active colloids at a finite distance. Scale bar: $10 \mu\text{m}$. Color bar: time, from the oldest positions (bright colors) to the latest positions (dark colors). **d**, Polarization fields in the vortex, meander and gas states. The dots indicate the location of the topological defects (Orange: +1, Blue: -1). Scale bar: 0.5 mm. **e**, Evolution of the number of topological defects $\mathcal{N}(t)$ during the coarsening process for $\Phi_o = 4\%$ (Polar liquid), $\Phi_o = 14\%$ (Meander), $\Phi_o = 34\%$ (Gas). The error in the number of defect measurement is smaller than the symbol size, see SI. **f**, Variations of the average number of topological defects in the steady state with the obstacle fraction. The meander phase emerges at $\Phi_c = 9 \pm 1\%$.

bend the dynamics of polar liquids into amorphous and singular flows while preserving local flocking motion.

We now establish that the meanders realize a dynamical vortex glass. To do so, we compare the flow orientations of fifty replicas of the very same experiment ($\Phi_o = 15\%$). We solely vary the initial conditions, keeping the colloid fraction and disorder realization identical. We then quantify the resemblance between the flow patterns by introducing a measure of the local overlap $q_{\alpha\beta}(\mathbf{r}) = \mathbf{p}_\alpha(\mathbf{r}) \cdot \mathbf{p}_\beta(\mathbf{r})$ between replicas α and β . Examples of overlap maps are shown in Fig. 3a for four different pairs of experiments, see also Supplementary Fig. S5. The replicated flows are identical when $q_{\alpha\beta}(\mathbf{r}) = +1$, opposite when $q_{\alpha\beta}(\mathbf{r}) = -1$ and orthogo-

nal when $q_{\alpha\beta}(\mathbf{r}) = 0$. A simple inspection of the maps readily indicates that, although all experiments correspond to overall different patterns, a few macroscopic regions are virtually identical from one replica to another. More quantitatively, we plot in Fig. 3c the distribution of the global overlap $\mathcal{Q}_{\alpha\beta} = \langle q_{\alpha\beta}(\mathbf{r}) \rangle_{\mathbf{r}}$, and compare it to that of the isolated vortex obtained in the flocking state. The two distributions are markedly different. In the flocking state, $P(\mathcal{Q}_{\alpha\beta})$ is composed of two symmetric peaks at $\mathcal{Q}_{\alpha\beta} = \pm 1$, as global circulation of either handedness are equally probable. Conversely, in the meander phase, $P(\mathcal{Q}_{\alpha\beta})$ is not symmetric. It is a broad Gaussian distribution centered around a positive mean value. In other words, even though disorder is isotropic

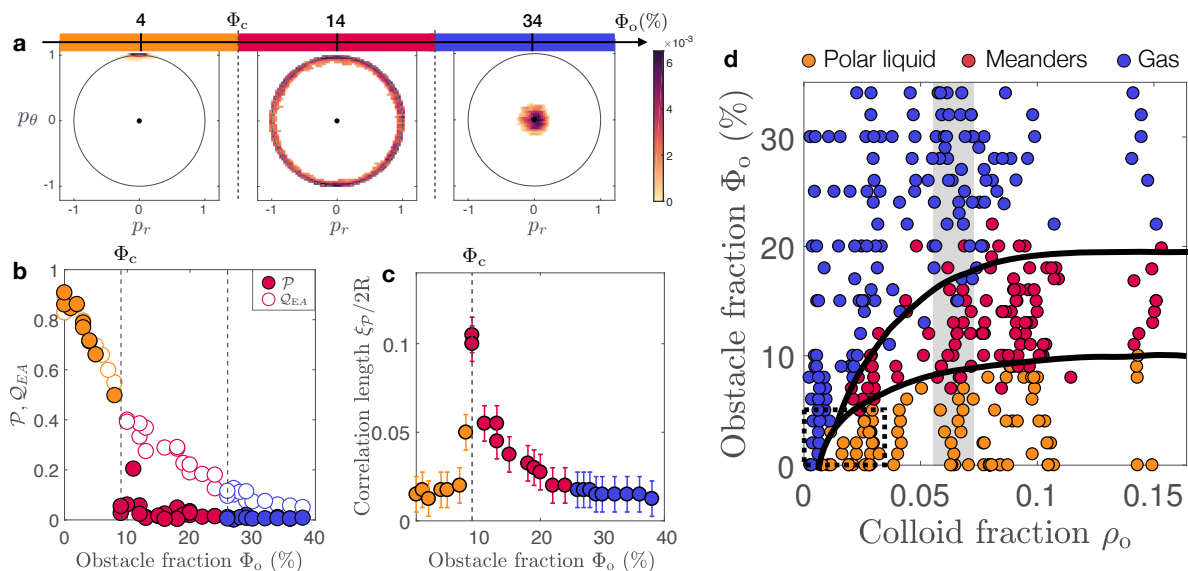


FIG. 2. **Suppression of long-range orientational order.** **a**, PDF of the polarization fields $P(p_r, p_\theta)$ in the three dynamical phases. Note that the distribution is isotropic but peaked along the unit circle in the meander phase: spontaneous flows are locally preserved but global polar order is suppressed by disorder. **b**, Variation of the global polarization \mathcal{P} and Edwards–Anderson Q_{EA} order parameters. In polar liquids $\mathcal{P} > 0$, in meanders $\mathcal{P} = 0$ but $Q_{EA} > 0$, and in a gas both \mathcal{P} and Q_{EA} vanish. **c**, Correlation length of the polarization field defined from the exponential decay of $\mathcal{P}(\ell)$ plotted in Supplementary Figure S1. The cusp of the $\xi_P(\Phi_o)$ curve at Φ_c hints towards a critical dynamical transition. The accuracy in the measurement of $\xi/2R$ is of the order of 10^{-2} . **d**, Phase diagram of polar active matter in isotropic disorder. The phase boundaries are equivalently determined from the number of topological defects (Fig. 1f), or from the variations of \mathcal{P} and Q_{EA} . In practice, we define the boundary separating the polar-liquid from the meander phase as $\mathcal{P} > 0.45$ and the boundary between the meander and gas phases as $\mathcal{P} < 0.45$ and $Q_{EA} > 0.2$. The geometry of the phase boundaries does not crucially depend on these criteria. The extent of the meander phase becomes vanishingly small only at the onset of the flocking transition. The dashed rectangle indicates the region of the phase diagram explored in [22] where the meander phase was missed. Orientational order is generically lost due to the emergence of meander patterns. The gray rectangle corresponds to the series of experiments discussed in the main text.

and homogeneous, the obstacles bias the orientation of the flow field over macroscopic regions of space, as a result reversing the orientation of the flow does not yield an equally probable pattern. The bias in the flow structure is clearly visible in the replica-averaged velocity field shown in Fig 3b.

Crucially, the large width of the overlap distribution demonstrates a broad range of meandering patterns that do not merely differ from each other by continuous distortions. The replicas are actually *topologically* inequivalent, as demonstrated by the distribution of the difference in the number of topological-defect between each pair of replicas ($\mathcal{N}_\alpha - \mathcal{N}_\beta$). The regions of the flow patterns that are robust to variations in the initial conditions are therefore shaped by pinned defects of identical charge and orientation which persist in all replicas. In other words, defects are strongly correlated in their spatially arrangements dictated by the local pattern of flow. This becomes evident upon inspecting the statistics of local overlap.

Unlike the global overlap distribution, $P(q_{\alpha\beta}(\mathbf{r}))$ is bimodal and sharply peaks at $q_{\alpha\beta}(\mathbf{r}) = \pm 1$, see Fig. 3e. Simply put, the meanders in each pair of replicas dif-

fer by the reversal of the flow orientation over a finite fraction of space. This area fraction is given by $1 - [P(q_{\alpha\beta} = +1) - P(q_{\alpha\beta} = -1)] \sim 0.5$, see also Supplementary Note III. We can then estimate the typical extent of the compact regions where the flow can flip sign from one replica to another by measuring the correlation length of the local overlap, or of the replica-averaged flow shown in Fig. 3f. We find that the overlap decorrelates exponentially over a finite distance $\xi_Q = 100 \pm 10 \mu\text{m}$. This finite correlation length implies that the meanders explore a conformational landscape including a number of steady states that scales as $\sim 2^{(R/\xi_Q)^2}$. The exponential degeneracy of the flows demonstrates that the meander phase is the dynamical analogue of a topological defect glass. It is strongly reminiscent of the vortex glass phases found in disordered flux lines in superconductors and in random-gauge Heisenberg magnets [28, 29, 41].

III. DYNAMICAL VORTEX GLASS AS A GAUGE GLASS

We now make more precise the connection between the DVG we observe here in active fluids and its static counterpart in superconductors. To do so, we build on a final

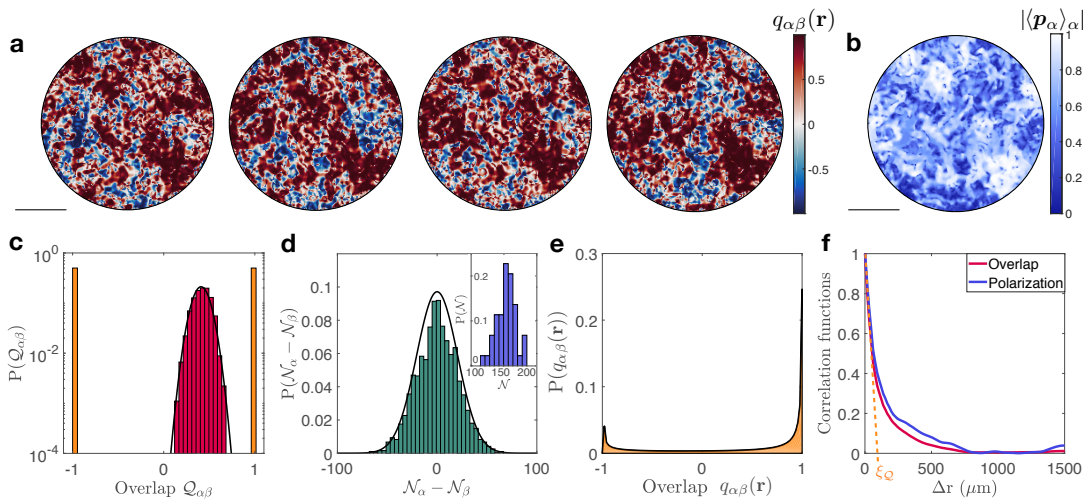


FIG. 3. **Meanders as dynamical vortex glasses.** **a**, Maps of the overlap field $q_{\alpha\beta}(\mathbf{r})$ for 4 out of 1225 different pairs of replicas (α, β). Scalebar: 1 mm. **b**, Magnitude of the replica-averaged polarization field. Disorder robustly sets the flow orientation in macroscopic regions (light colors). Scalebar: 1 mm. **c**, Overlap distributions in the polar liquid and meander phases. In the polar liquid phase (light orange) the distribution is symmetric and bimodal. Clockwise and counterclockwise vortices are equiprobable. In the meander phase, the distribution is a wide Gaussian centered on 0.46. **d**, Distribution of the difference between the number of topological defects in each pair of replicas. The distribution is a Gaussian with a standard deviation $\sigma = 18 \pm 3$ much larger than the uncertainty defined by the standard deviation of the topological charge (which should be constrained to equal 1 in a circular geometry). Inset: distribution of the number of defects in each replica. The replicated flows are topologically distinct. **e**, Probability density of the local overlap $q_{\alpha\beta}(\mathbf{r})$. The distribution is asymmetric but sharply peaked at ± 1 . Locally the active fluid either flows along identical or opposite directions in each replica of the same experiment. **f**, Decay of the spatial correlation of $q_{\alpha\beta}(\mathbf{r})$ averaged over all replicas and of the replica-averaged polarization field plotted in (b). Both decorrelations occur over the same finite distance $\xi_Q = 100 \pm 10 \mu\text{m}$. All panels correspond to experiments performed deep in the meander phase $\Phi_o = 15\%$.

set of experiments performed in periodic lattices of obstacles. A systematic investigation reveals that no meander forms in the absence of disorder, see Supplementary Note IV. The spatial heterogeneities in the local obstacle fraction $\phi_o(\mathbf{r})$ are essential to generate the meandering flow patterns. At lowest order in gradients, disorder thus minimally alters Toner–Tu hydrodynamics for the conserved roller density ρ and the flow velocity \mathbf{v} [1, 34],

$$\begin{aligned} \partial_t \rho &= -\nabla \cdot (\rho \mathbf{v}), \\ \partial_t \mathbf{v} + \lambda \mathbf{v} \cdot \nabla \mathbf{v} &= (a_2 - a_4 |\mathbf{v}|^2) \mathbf{v} + K \nabla^2 \mathbf{v} - \beta \nabla \rho - \beta_o \nabla \phi_o, \end{aligned} \quad (1)$$

All the transport coefficients are taken to be constant positive parameters. When $\nabla \phi_o = \mathbf{0}$, Eq. 1 reduces to the standard Toner–Tu equations, which quantitatively predicts the vortical flows of Fig. 1a [32]. The potential terms a_2, a_4 set the mean value of the flow velocity ($|\mathbf{v}| = \sqrt{a_2/a_4} \equiv v_0$) deep in the homogeneous ordered phase, while λ controls self-advection and the elastic constant K penalizes flow distortions. The β_o term functions similar to the inverse compressibility β and reflects the coupling to disorder, providing a direct qualitative explanation for the bias of the overlap distribution in Fig. 3c. Although the obstacles are isotropic and, on average, homogeneously distributed, $\phi_o(\mathbf{r})$ acts as a random pressure field that locally drives the flows along the same

obstacle-depleted regions in all replicas. For weak disorder ($\Phi_o < \Phi_c$), the ordered flows are only marginally perturbed by the obstacles, and we can perform a simple linearized analysis about the polarized state. Deep in the ordered state, we have $\mathbf{v} = v_0(\cos \theta, \sin \theta)$, with θ as the soft Goldstone mode. As detailed in Supplementary Note V, for $\theta \ll 1$, we Fourier transform ($\theta_{\mathbf{q}} = \int d\mathbf{r} \theta(\mathbf{r}) e^{-i\mathbf{q}\cdot\mathbf{r}}$) and obtain the steady state orientational correlator within linear response to be

$$\overline{\theta_{\mathbf{q}}^2} = \frac{\beta_o^2 \Phi_o q_x^2 q_y^2}{[(c_{\parallel} v_0 q_x^2 - c_{\perp}^2 q_y^2)^2 + v_0^2 K^2 q_x^2 q_y^4]}, \quad (2)$$

where $c_{\parallel} = \lambda v_0$ and $c_{\perp} = \sqrt{\beta \rho_0}$ are the longitudinal and transverse sound speeds respectively, with ρ_0 being the mean colloidal roller fraction and $q = |\mathbf{q}|$. The overbar denotes a disorder average. Velocity fluctuations hence remain finite on large scales (signalling true long-range order) and only linearly suppress the mean polarization by a term $\propto \Phi_o$, in agreement with our experimental measurements in the small disorder limit ($\Phi_o < \Phi_c$), see Fig. 2c and Supplementary Note V.

For strong disorder, we have to go beyond this linearized spin-wave theory and account for both nonlinearities and the presence of topological defects. Before we proceed it is worth recalling the basic physics of defect-driven phase transitions in both passive and active sys-

tems. In pure two-dimensional (2D) systems, such as superfluid, liquid crystal or magnetic films at equilibrium, defect unbinding is driven by entropic effects which scale as $\sim T \ln R$ in a system of size R . At high enough temperature T , entropy eventually overwhelms the equally divergent elastic energy cost of creating an isolated defect $\sim K \ln R$. This is the essence of the Kosterlitz-Thouless argument [42, 43]. A similar mechanism is also at play in 2D *active* nematics, where activity induced defect self-propulsion [14] essentially plays the role of an enhanced effective temperature that governs the defect unbinding transition [15]. An important ingredient in all the above cases is that the ordered state only supports *quasi-long ranged order* that allows elasticity and fluctuations (active or thermal) to compete on the same footing. In stark contrast, ordered polar flocks exhibit genuine long-ranged order in 2D [4, 34]. As a result, fluctuations are dramatically suppressed on large scales and the usual Kosterlitz-Thouless argument becomes unavailable. Hence topological defects in clean polar flocks do not spontaneously unbind as in active nematics and only participate in a rapid coarsening process by annihilating quickly to yield pristine ordered flow, as evidenced in Fig. 1a.

Disorder changes this picture in important ways. As we show below and in Supplementary Notes VI and VII, quenched fluctuations due to the random obstacles can provide an additional contribution that competes with orientational elasticity to uncover a new active defect-unbinding scenario. For simplicity, we will fix the colloidal roller density to be a constant ($\rho = \rho_0$) and address the effects of density variations elsewhere. In a maximally polarized fluid, we neglect any fast fluctuations of the speed and focus only on the hydrodynamic mode, the orientation θ . Retaining the full nonlinear dependence on θ , we find that at long-wavelengths the convective nonlinearities solely compete with the random pressure term in Eq. 1. To gain some insight on this competition, let us first consider a local minimum of $\phi_o(\mathbf{r})$ at the origin, the inward disorder pressure must be balanced by a centrifugal kinematic pressure $\sim \lambda v^2/r$ associated with an azimuthal flow. Along with $\nabla \cdot \hat{\mathbf{v}} = 0$ from the continuity equation with constant density ρ_0 , this competition then constrains the angular fluctuations to obey,

$$\nabla \theta = -\frac{\beta_o}{\lambda v_0^2} \hat{\mathbf{z}} \times \mathbb{P} \cdot \nabla \phi_o \equiv \mathcal{A}(\mathbf{r}) , \quad (3)$$

where $\mathbb{P} = \mathbf{1} - \hat{\mathbf{v}}\hat{\mathbf{v}}$. Remarkably, this quenched distribution of phase distortions is reminiscent of random-gauge XY models, and flux-line glasses in type II superconductors, see e.g. [27–29]. Active self-advection nonlinearly transforms the quenched disorder potential ϕ_o into an effective random $U(1)$ gauge field \mathcal{A} , whose local circulation

$$Q(\mathbf{r}) = \hat{\mathbf{z}} \cdot [\nabla \times \mathcal{A}(\mathbf{r})] , \quad (4)$$

now defines the *quenched* topological charge in the background. The polar fluid hence navigates the obstacles,

generating meanders dictated by \mathcal{A} , while elasticity penalizes these distortions. For a given disorder configuration, the flow streamlines on large scales must satisfy the nonlinear constraint in Eq. 3, which can be used to obtain (see Supplementary Note VI for details) the steady state distribution of θ to be $P[\theta(\mathbf{r})] \propto \lim_{T \rightarrow 0} \exp(-E/T)$ with an auxiliary “temperature” T and an effective energy

$$E[\theta(\mathbf{r})] = \frac{K}{2} \int d^2r |\nabla \theta - \mathcal{A}(\mathbf{r})|^2 , \quad (5)$$

whose zero temperature ($T \rightarrow 0$) ground state controls the flow configurations of the disordered flock. This completes our mapping of the nonlinear meandering flows in a polar fluid on a disordered substrate to the well known problem of finding the ground states of a random-gauge XY model [27, 29, 44].

The effective energy in Eq. 5 captures the competition between elastic restoring forces and disorder which immediately allows a Kosterlitz-Thouless style argument for proliferating free vortices (Supplementary Note VII). The elastic penalty of an isolated defect $\sim K \ln(R/a)$ (a is a core size) can be offset by the energy gain $\sim K \Phi_o(\beta_o/\lambda v_0^2) \ln(R/a)$ from optimally screening out the background charge. Their balance hence predicts a critical threshold $\Phi_c \propto \lambda v_0^2/\beta_o$ beyond which pinned vortices proliferate, in agreement with our experimental findings. A more sophisticated analysis including renormalization corrections to the elastic constant is presented in Supplementary Note VII. This rationalizes the existence of the dynamical vortex glass phase along with its phase transition as being driven by the disorder driven unbinding of defects. Before we close, we briefly comment on the role of activity in our analysis. Note that, although we obtain an equilibrium-like mapping in Eq. 5, activity was crucial in generating the gauge field \mathcal{A} via self-advection. Additionally, the effective energy only controls the static properties of the system, dynamical correlators may continue to exhibit violations of detailed balance. Higher order nonlinear active terms neglected here could also spoil the simple equilibrium mapping when including fluctuation corrections, a feature worth exploring in the future.

IV. CONCLUDING REMARKS

In conclusion, combining high-content experiments and theory we have shown how dynamical vortex glasses generically emerge when the polar order of flocking matter competes with isotropic disorder. We emphasize the generality of our predictions. Both the topological-defect stabilisation scenario and the extensive complexity of the flow patterns solely rely on stable uniaxial order in a fluid assembled from motile units. Beyond the specifics, of colloidal active matter, we therefore expect dynamical vortex glasses to emerge in a host of active materials ranging from confined microtubule nematics [11], to concentrated bacteria suspensions [37], and cell tissues [45] cruising through disorder. Establishing a quantitative theory of their amorphous patterns remains a formidable challenge.

-
- [1] John Toner, Yuhai Tu, and Sriram Ramaswamy, “Hydrodynamics and phases of flocks,” *Annals of Physics* **318**, 170 – 244 (2005), special Issue.
- [2] M. C. Marchetti, J. F. Joanny, S. Ramaswamy, T. B. Liverpool, J. Prost, Madan Rao, and R. Aditi Simha, “Hydrodynamics of soft active matter,” *Rev. Mod. Phys.* **85**, 1143–1189 (2013).
- [3] Andrea Cavagna and Irene Giardina, “Bird flocks as condensed matter,” *Annu. Rev. Condens. Matter Phys.* **5**, 183–207 (2014).
- [4] Hugues Chaté, “Dry aligning dilute active matter,” *Annual Review of Condensed Matter Physics* **11**, 189–212 (2020).
- [5] Volker Schaller, Christoph Weber, Christine Semmrich, Erwin Frey, and Andreas R Bausch, “Polar patterns of driven filaments,” *Nature* **467**, 73 (2010).
- [6] Antoine Bricard, Jean-Baptiste Caussin, Nicolas Desreumaux, Olivier Dauchot, and Denis Bartolo, “Emergence of macroscopic directed motion in populations of motile colloids,” *Nature* **503** (2013).
- [7] Jing Yan, Ming Han, Jie Zhang, Cong Xu, Erik Luijten, and Steve Granick, “Reconfiguring active particles by electrostatic imbalance,” *Nature materials* **15**, 1095 (2016).
- [8] Jie Zhang, Erik Luijten, Bartosz A. Grzybowski, and Steve Granick, “Active colloids with collective mobility status and research opportunities,” *Chem. Soc. Rev.* **46**, 5551–5569 (2017).
- [9] Julien Deseigne, Sébastien Léonard, Olivier Dauchot, and Hugues Chaté, “Vibrated polar disks: spontaneous motion, binary collisions, and collective dynamics,” *Soft Matter* **8**, 5629–5639 (2012).
- [10] Nitin Kumar, Harsh Soni, Sriram Ramaswamy, and AK Sood, “Flocking at a distance in active granular matter,” *Nature Communications* **5** (2014).
- [11] Amin Doostmohammadi, Jordi Ignés-Mullol, Julia M Yeomans, and Francesc Sagués, “Active nematics,” *Nature communications* **9**, 1–13 (2018).
- [12] Suraj Shankar, Sriram Ramaswamy, and M Cristina Marchetti, “Low-noise phase of a two-dimensional active nematic system,” *Physical Review E* **97**, 012707 (2018).
- [13] Tim Sanchez, Daniel T. N. Chen, Stephen J. DeCamp, Michael Heymann, and Zvonimir Dogic, “Spontaneous motion in hierarchically assembled active matter,” *Nature* **491**, 431–434 (2012).
- [14] Luca Giomi, Mark J Bowick, Xu Ma, and M Cristina Marchetti, “Defect annihilation and proliferation in active nematics,” *Physical review letters* **110**, 228101 (2013).
- [15] Suraj Shankar, Sriram Ramaswamy, M Cristina Marchetti, and Mark J Bowick, “Defect unbinding in active nematics,” *Physical review letters* **121**, 108002 (2018).
- [16] John A Blackman and J Tagüeña, *Disorder in condensed matter physics: a volume in honour of Roger Elliott* (Oxford University Press, USA, 1991).
- [17] Pierre-Gilles De Gennes, *Superconductivity of metals and alloys* (CRC Press, 2018).
- [18] George W Crabtree and David R Nelson, “Vortex physics in high-temperature superconductors,” *Physics Today* **50**, 38–45 (1997).
- [19] Oleksandr Chepizhko, Eduardo G. Altmann, and Fernando Peruani, “Optimal noise maximizes collective motion in heterogeneous media,” *Phys. Rev. Lett.* **110**, 238101 (2013).
- [20] David A Quint and Ajay Gopinathan, “Topologically induced swarming phase transition on a 2d percolated lattice,” *Physical biology* **12**, 046008 (2015).
- [21] Clemens Bechinger, Roberto Di Leonardo, Hartmut Löwen, Charles Reichhardt, Giorgio Volpe, and Giovanni Volpe, “Active particles in complex and crowded environments,” *Reviews of Modern Physics* **88**, 045006 (2016).
- [22] Alexandre Morin, Nicolas Desreumaux, Jean-Baptiste Caussin, and Denis Bartolo, “Distortion and destruction of colloidal flocks in disordered environments,” *Nature Physics* **13**, 63 (2017).
- [23] Rakesh Das, Manoranjan Kumar, and Shradha Mishra, “Polar flock in the presence of random quenched rotators,” *Phys. Rev. E* **98**, 060602 (2018).
- [24] CJ Olson Reichhardt and Charles Reichhardt, “Avalanche dynamics for active matter in heterogeneous media,” *New Journal of Physics* **20**, 025002 (2018).
- [25] John Toner, Nicholas Guttenberg, and Yuhai Tu, “Swarming in the dirt: Ordered flocks with quenched disorder,” *Phys. Rev. Lett.* **121**, 248002 (2018).
- [26] John Toner, Nicholas Guttenberg, and Yuhai Tu, “Hydrodynamic theory of flocking in the presence of quenched disorder,” *Phys. Rev. E* **98**, 062604 (2018).
- [27] Michael Rubinstein, Boris Shraiman, and David R Nelson, “Two-dimensional xy magnets with random dzyaloshinskii-moriya interactions,” *Physical Review B* **27**, 1800 (1983).
- [28] Thomas Nattermann and Stefan Scheidl, “Vortex-glass phases in type-II superconductors,” *Advances in Physics* **49**, 607–704 (2000).
- [29] David Carpentier and Pierre Le Doussal, “Topological transitions and freezing in xy models and coulomb gases with quenched disorder: renormalization via traveling waves,” *Nuclear Physics B* **588**, 565–629 (2000).
- [30] G. Quincke, “Über rotationen im constanten electrischen felde,” *Annalen der Physik* , 417–486 (1896).
- [31] Oleg D Lavrentovich, “Active colloids in liquid crystals,” *Current opinion in colloid & interface science* **21**, 97–109 (2016).
- [32] Antoine Bricard, Jean-Baptiste Caussin, Debasish Das, Charles Savoie, Vijayakumar Chikkadi, Kyohei Shitara, Oleksandr Chepizhko, Fernando Peruani, David Saintillan, and Denis Bartolo, “Emergent vortices in populations of colloidal rollers,” *Nature communications* **6**, 7470 (2015).
- [33] Delphine Geyer, David Martin, Julien Tailleur, and Denis Bartolo, “Freezing a flock: Motility-induced phase separation in polar active liquids,” *Physical Review X* **9**, 031043 (2019).
- [34] John Toner and Yuhai Tu, “Long-range order in a two-dimensional dynamical XY model: How birds fly together,” *Phys. Rev. Lett.* **75**, 4326–4329 (1995).
- [35] Maria Zeitz, Katrin Wolff, and Holger Stark, “Active brownian particles moving in a random lorentz gas,” *The European Physical Journal E* **40**, 23 (2017).

- [36] Alexandre Morin, David Lopes Cardozo, Vijayakumar Chikkadi, and Denis Bartolo, “Diffusion, subdiffusion, and localization of active colloids in random post lattices,” *Phys. Rev. E* **96**, 042611 (2017).
- [37] Hugo Wioland, Enkeleida Lushi, and Raymond E Goldstein, “Directed collective motion of bacteria under channel confinement,” *New Journal of Physics* **18**, 075002 (2016).
- [38] Kun-Ta Wu, Jean Bernard Hishamunda, Daniel TN Chen, Stephen J DeCamp, Ya-Wen Chang, Alberto Fernández-Nieves, Seth Fraden, and Zvonimir Dogic, “Transition from turbulent to coherent flows in confined three-dimensional active fluids,” *Science* **355**, eaal1979 (2017).
- [39] Achini Opathalage, Michael M Norton, Michael PN Juniper, Blake Langeslay, S Ali Aghvami, Seth Fraden, and Zvonimir Dogic, “Self-organized dynamics and the transition to turbulence of confined active nematics,” *Proceedings of the National Academy of Sciences* **116**, 4788–4797 (2019).
- [40] Andrea Cavagna, “Supercooled liquids for pedestrians,” *Physics Reports* **476**, 51–124 (2009).
- [41] Matthew P. A. Fisher, “Vortex-glass superconductivity: A possible new phase in bulk high- t_c oxides,” *Phys. Rev. Lett.* **62**, 1415–1418 (1989).
- [42] John Michael Kosterlitz and David James Thouless, “Ordering, metastability and phase transitions in two-dimensional systems,” *Journal of Physics C: Solid State Physics* **6**, 1181 (1973).
- [43] JM Kosterlitz, “The critical properties of the two-dimensional xy model,” *Journal of Physics C: Solid State Physics* **7**, 1046 (1974).
- [44] David Carpentier and Pierre Le Doussal, “Disordered xy models and coulomb gases: renormalization via traveling waves,” *Physical review letters* **81**, 2558 (1998).
- [45] G Duclos, C Blanch-Mercader, V Yashunsky, G Salbreux, J-F Joanny, J Prost, and Pascal Silberzan, “Spontaneous shear flow in confined cellular nematics,” *Nature physics* **14**, 728–732 (2018).
- [46] Delphine Geyer, Alexandre Morin, and Denis Bartolo, “Sounds and hydrodynamics of polar active fluids,” *Nature materials* **17**, 789–793 (2018).
- [47] J. R. Melcher and G. I. Taylor, “Electrohydrodynamics: A review of the role of interfacial shear stresses,” *Annual Review of Fluid Mechanics* **1**, 111–146 (1969).
- [48] Peter J Lu, Peter A Sims, Hidekazu Oki, James B Macarthur, and David A Weitz, “Target-locking acquisition with real-time confocal (tarc) microscopy,” *Optics express* **15**, 8702–8712 (2007).
- [49] John C Crocker and David G Grier, “Methods of digital video microscopy for colloidal studies,” *Journal of colloid and interface science* **179**, 298–310 (1996).
- [50] D. Blair and E. Dufresne, “The matlab particle tracking code repository,” .

METHODS

A. Quincke rollers experiments

The experimental setup is similar to that described in [46]. We disperse polystyrene colloids of radius $a =$

$2.4\ \mu\text{m}$ (Thermo Scientific G0500) in a solution of hexadecane including 5.5×10^{-2} wt % of dioctyl sulfosuccinate sodium salt (AOT). We then inject the solution in microfluidic chambers made of two electrodes spaced by a $25\ \mu\text{m}$ -thick scotch tape. The electrodes are glass slides, coated with indium tin oxide (Solems, ITOSOL30, thickness: 80 nm). We let the colloids sediment on the bottom electrode and apply a DC voltage of 120 V. The resulting electric field triggers the so-called Quincke electro-rotation and causes the colloids to roll at a constant speed $v_0 = 0.8\ \text{mm/s}$ [6, 47]. The microfluidic device is sketched in . 1b. We confine the colloidal rollers inside circular chambers of radius $R = 1.5\ \text{mm}$ including random lattices of circular posts of radius $10\ \mu\text{m}$. Both the obstacles and the confining disks are made of a $2\ \mu\text{m}$ -thick layer of insulating photoresist resin (Microposit S1818) patterned by means of conventional UV-Lithography as explained in [22]. The patterns are lithographed on the bottom electrode. Note that the distribution of the obstacle centers corresponds to a planar Poisson process, the circular posts can therefore overlap as see in Fig. 1b and Movie S3. The experiments reported in the main text correspond to thirty different microfluidic chambers including obstacle fractions ranging from 0 % to 38 %. We fine tune the mean roller fraction ρ_0 using a T-junction to inject sequentially a colloidal suspension or a colloid-free solvent.

If not specified otherwise, the stationary flows are measured in the first chamber 120 s after the application of the DC field. This waiting time is more than one order of magnitude larger than the flows’ relaxation time, see Supplementary Note I. For the replica experiments we proceed as follows: the chambers are filled with the colloids at the desired area fraction. We motorize the colloids, wait for 120 s and film their motion for 5 s. We then switch the voltage off, and switch it on again repeating the same procedure fifty times in a row.

B. From Lagrangian trajectories to Eulerian flow fields

In order to track of the trajectories of the rollers, we image them with a Nikon AZ100 microscope with a 4.8X magnification and record videos with a CMOS camera (Basler Ace) at 190 fps. All measurements are systematically repeated three times for different initial conditions and same disorder configuration. If not specified otherwise, we measure all quantities reported in the main text after the ensemble of rollers has reached its stationary state.

1. Lagrangian trajectories

We detect the position of all the rollers with a sub-pixel accuracy using the algorithm introduced by Lu et al in [48]. We then reconstruct their trajectories over the

whole 3 mm wide circular chambers using the Crocker and Grier algorithm [49] with the MATLAB routine available at [50]. We define the individual roller velocities from their displacements over two subsequent frames (time interval: $\delta t = 5.3$ ms): $\mathbf{v}_i(t) = \mathbf{r}_i(t + \delta t) - \mathbf{r}_i(t)$, where $\mathbf{r}_i(t)$ and $\mathbf{v}_i(t)$ are respectively the position and velocity of particule i at time t . The accuracy of the position measurements is of the order of $0.1 \mu\text{m}$, inducing an accuracy of the order of $40 \mu\text{m/s}$ for individual speed measurements. When powered with an electric field \mathbf{E} of magnitude 120 V, all colloids roll at a constant speed:

$$v_0 = 0.80 \pm 0.04 \text{ mm/s}. \quad (6)$$

In addition, when isolated, their direction of motion freely diffuses on the unit circle with a rotational diffusivity D_R defined as the exponential decorrelation rate of the velocity orientation in an isotropic phase:

$$D_R = 2.2 \pm 0.1 \text{ s}^{-1}. \quad (7)$$

2. Eulerian fields

Building on these Lagrangian measurements, we reconstruct the instantaneous Eulerian velocity fields $\mathbf{v}(\mathbf{r}, t)$ as follows. We average the instantaneous roller velocities in $76.4 \mu\text{m} \times 76.4 \mu\text{m}$ binning windows arranged on a square lattice with a lattice spacing of $15.3 \mu\text{m}$. Given the roller density, each PIV window typically averages the velocity of 25 rollers. We systematically checked that none of our results crucially depends on the specific choice of the size of the binning windows. The polarization and over-

lap fields are computed with the same spatial resolution from $\mathbf{v}(\mathbf{r}, t)$.

To compute the polarization order parameter from the instantaneous velocity field, we first average the radial and azimuthal components of the polarization field $\mathbf{p}(\mathbf{r}) \equiv \langle \hat{\mathbf{v}}(\mathbf{r}, t) \rangle_t$ over square boxes of size ℓ . We then compute the spatial average: $\mathbf{p}_B \equiv (\langle p_r(\mathbf{r}) \rangle_{\mathbf{r}}, \langle p_\theta(\mathbf{r}) \rangle_{\mathbf{r}})$, in each box B . Finally, $\mathcal{P}(\ell)$ corresponds to the norm of \mathbf{p}_B averaged over all boxes B .

Acknowledgements. We acknowledge support from ANR program WTF and IDEX program ToRe. M. C. M. was supported by the US National Science Foundation through award DMR-1609208. S. S. is supported by the Harvard Society of Fellows. We thank D. Carpentier, O. Dauchot, W. T. M. Irvine, and A. Morin for insightful comments and suggestions.

Data availability The data that support the plots within this paper and other findings of this study are available from the corresponding author upon request.

Author Contributions D. B. conceived the project. A. C. and D. B. designed the experiments. A. C. performed the experiments and analyzed data. A. C. and D. B. interpreted and discussed the experiments. M. C. M. and S. S. performed the theory. All authors discussed the results and wrote the manuscript. A. C. and S. S. contributed equally.

Author Information Correspondence and requests for materials should be addressed to D. B. (email: denis.bartolo@ens-lyon.fr).

Competing interests The authors declare no competing interests.